Published in final edited form as:
Magn Reson Med. 2002 March ; 47(3): 433–438.

Combined MR Proton Lung Perfusion/Angiography and Helium Ventilation:

Potential for Detecting Pulmonary Emboli and Ventilation Defects

Jie Zheng[1,*], **Jason C. Leawoods**[2], **Mark Nolte**[1], **Dmitriy A. Yablonskiy**[1,2], **Pamela K. Woodard**[1], **Gerhardt Laub**[3], **Robert J. Gropler**[1], and **Mark S. Conradi**[1,2]

1*Mallinckrodt Institute of Radiology, Washington University School of Medicine, St. Louis, Missouri*

2*Department of Physics, Washington University, St. Louis, Missouri*

3*Siemens Medical Systems, Chicago, Illinois*

Abstract

Three-dimensional (3D) perfusion imaging allows the assessment of pulmonary blood flow in parenchyma and main pulmonary arteries simultaneously. MRI using laser-polarized ^{3}He gas clearly shows the ventilation distribution with high signal-to-noise ratio (SNR). In this report, the feasibility of combined lung MR angiography, perfusion, and ventilation imaging is demonstrated in a porcine model. Ultrafast gradient-echo sequences have been used for 3D perfusion and angiographic imaging, in conjunction with the use of contrast agent injections. 2D multiple-section ^{3}He imaging was performed subsequently by inhalation of 450 ml of hyperpolarized ^{3}He gas. The MR techniques were examined in a series of porcine models with externally delivered pulmonary emboli and/or airway occlusions. With emboli, perfusion deficits without ventilation defects were observed; airway occlusion resulted in matched deficits in perfusion and ventilation. High-resolution MR angiography can unambiguously reveal the location and size of the blood emboli. The combination of the three imaging methods may provide complementary information on abnormal lung anatomy and function.

Keywords

pulmonary emboli; MR perfusion; MR angiography; hyperpolarized gas; contrast agents

The development of high-speed gradient systems and fast imaging methods has permitted ultrafast contrast-enhanced lung perfusion imaging with subsecond temporal resolution and millimeter spatial resolution (1-8). Imaging of the lung parenchyma suffers from low proton density, physiological motion (cardiac and respiratory motion adjacent to the lung), and short T_2^* from local magnetic field inhomogeneity due to multiple interfaces of air and soft tissues (3,9-12); significantly reduced times TR and TE in the gradient-echo sequence allow dramatically improved SNR. Recently, bolus injection of gadolinium contrast agent in conjunction with an ultrafast 3D gradient-echo sequence has demonstrated volumetric lung parenchymal perfusion images with 2-3 sec temporal resolution (7). This technique allows simultaneous evaluation of lung perfusion and flow in the major pulmonary vasculature. On the other hand, submillimeter high-spatial-resolution pulmonary angiography has been achieved with bolus administration of gadolinium contrast agent and first-pass MR data acquisition during the arterial phase of the contrast agent (13-15). This contrast-enhanced

*Correspondence to: J. Zheng, Mallinckrodt Institute of Radiology, Washington University School of Medicine, 510 S. Kings Highway, Box 8225, St. Louis, MO 63110. E-mail: zhengj@mir.wustl.edu

pulmonary angiography shows high SNR and can depict pulmonary arteries beyond the subsegmental branches. Integration of perfusion and angiography may allow better evaluation of parenchymal blood flow states and vasculature involvement; this is particularly interesting when pulmonary emboli are studied (10,16).

The ability of MR to image the lung air space is important for the diagnosis of a variety of pulmonary ventilation abnormalities. Recently, assessment of regional lung ventilation using hyperpolarized noble gas has emerged as an imaging technique for evaluating patients with lung disease, such as tumor, emphysema, bronchiectasis, cystic fibrosis, and asthma (17-24). Compared to O_2-enhanced lung MRI (25,26), which has the advantage of needing no special equipment, ^{3}He MRI provides high SNR and contrast-to-noise ratio (CNR), with image intensity directly proportional to the local concentration of inhaled ^{3}He. It has long been recognized that both pulmonary perfusion and ventilation images are needed to identify and distinguish certain lung diseases. For example, mismatched and matched perfusion/ventilation defects can be found in pulmonary embolism and chronic obstructive pulmonary disease (COPD) patients, respectively. Some efforts have been made (27) to evaluate such perfusion/ventilation defects in a porcine model using contrast-enhanced perfusion imaging and oxygen-enhanced ventilation imaging approaches. Another method using ^{3}He itself for dynamic measurement of lung perfusion as well as ventilation has also been reported (28). To date, however, MR techniques using proton and ^{3}He imaging to visualize lung structure have only been reported for assessing perfusion and ventilation in rat lungs (29).

In this report, we show the feasibility of combining three MR techniques for evaluation of the lung function in a porcine model with appropriate spatial resolution and volume coverage. To our knowledge, this is the first time that MR perfusion, ventilation, and angiography have been combined to assess lung function. To demonstrate the utility of the techniques, pulmonary and ventilation defects were created in the animals and both matched and mismatched perfusion/ventilation defects were demonstrated.

MATERIALS AND METHODS

Animal Models

Animal Preparation—Eight domestic pigs (weight 23.6 ± 2.7 kg) were used for this study. The pigs were premedicated by intramuscular injection of atropine (0.05 mg/kg), xylazine (2 mg/kg), and ketamine (20 mg/kg). An intravenous access line was secured in the ear for contrast agent injection and for hydration of the animal. The pigs were then anesthetized with intravenous injections of pentobarbital (25 mg/kg) and underwent endotracheal intubation. A 9-F Pinnacle introducer sheath (Medi-Tech, Watertown, MA) was inserted through the right internal jugular vein to the superior vena cava (SVC) in some animals for delivery of blood clots to create artificial pulmonary emboli.

After preparation the pigs were placed supine in the magnet bore and mechanically ventilated through a small animal ventilator (Harvard Apparatus, South Natick, MA) at a rate of 15 breaths/min, a stroke of 300 ml, and an inspiration/ expiration time ratio of 40 / 60. Normal saline (0.9%) was administered throughout the MR procedure through the established intravenous line at the rate of 3 ml/kg/hr to maintain hydration. Anesthesia was maintained using a mixture of isoflurane/oxygen ventilation during the imaging procedure. Blood O_2 saturation, pulse rate, end tidal CO_2, and temperature of the pig was monitored throughout the procedure. A 4-lead ECG patch was attached on the chest of the pig. For breathhold scans, ventilation was stopped with the animal's diaphragm in the inspiration position. All animal experiments were approved by the Animal Study Committee of our institute.

Embolism Preparation (n = 5)—The creation of emboli has been described previously (30). In brief, 20 ml of fresh porcine blood was withdrawn from the internal jugular vein and placed in a polyvinyl chloride tube of 10 mm internal diameter. The tube was sealed and placed on a turntable rotating at 16 revolutions per second for 30-60 min until a thrombus was formed. The large thrombus was then removed from the tube and cut into smaller segments with a diameter of 3 mm and varying lengths from 1-4 cm. To deliver the segments to the pulmonary vessels in the animal, the segments were inserted into a 1-ml syringe and then injected into the 9-F catheter, flushing with normal saline.

Bronchi Obstruction (n = 3)—An 8-F balloon catheter was used to block one of the bronchial branches. A small amount of diluted gadolinium contrast agent was first infused into the balloon for MRI visualization of the location of the catheter and partial dilation of the balloon. The catheter was then inserted into the lung of the animal through the endotracheal tube and extended into either the right or the left lung. After sensing resistance of the catheter in the lung, the balloon was then inflated completely to fully block the airway. A 3D proton FLASH image was acquired afterwards to identify the location of the balloon.

MR Perfusion and Angiographic Imaging

The MR system is a 1.5 T Magnetom Sonata system (Siemens Medical Systems, Erlangen, Germany) with a high-performance gradient system (maximum gradient strengths of 40 mT/m and maximum slew rate of 200 mT/m/msec). The perfusion images were obtained using a 3D gradient-echo sequence with asymmetric *k*-space sampling in readout, phase-encoding, and partition-encoding directions. The strategies to reduce the scan time include moving the symmetric *k*-space to one side (20%) along the phase-encoding direction and zero-filling the rest of *k*-space. In the slice direction, sinc interpolation is applied to increase the slice display by a factor of 2. A rectangular RF pulse with a duration of 100 μsec was used, allowing TR and TE to be shortened to 1.64 and 0.6 msec, respectively. Other imaging parameters included: flip angle = 15°, readout bandwidth = 1295 Hz/pixel, in-plane field of view (FOV) = 320 × 200 mm^2 and slab thickness = 80 mm, data acquisition matrix = 256 × 120 and 12 partitions (interpolated to 24), with a voxel size of 1.3 × 1.7 × 3.3 mm^3. The orientation of the 3D slab was oblique coronal to transverse to fully cover both lungs. The temporal resolution was 1.98 sec per 3D dataset with a total of 13 datasets collected continuously during the first-pass of the contrast agent. The 3D perfusion sequence was designed to perform online subtraction (subtracting the first 3D dataset from all later datasets) and to reconstruct automatically a MIP (maximum intensity projection) image for each subtracted 3D dataset. For 13 total sets there were 12 subtracted datasets and the total reconstruction time was approximately 7 min.

High-spatial-resolution 3D angiography was obtained by another 3D gradient-echo sequence with the same *k*-space sampling scheme and a TR/TE of 3.2/1.1 msec. The readout bandwidth was 432 Hz / pixel and the flip-angle was 30°. The 3D slab was prescribed in the same location as in the perfusion study. The data acquisition matrix was 512 × 243 × 96 (interpolated partition number), resulting in a voxel size of 0.66 × 0.82 × 0.83 mm^3. Scanning time for the angiography measurement was 25 sec. The angiographic MR differs from the perfusion MR primarily in being higher spatial resolution and requiring a longer time to acquire a 3D dataset. MIP images, as well as MPR (multiplanar reconstruction) images, were obtained to assist visualization of pulmonary arteries and emboli.

To perform the contrast-enhanced perfusion study, a single dose of 0.1 mmol/kg gadopenetate dimeglumine (Magnevist; Schering-Plough, Erlangen, Germany) or gadodiamide (Omniscan; Nycomed Imaging, Oslo, Norway) was injected through the established ear vein catheter as a bolus in 2 sec, followed by a 10-ml saline flush. The injection was performed after the first 3D dataset was acquired. For the angiographic acquisition, the same agent with a doubled dose of

0.2 mmol/kg was injected over 20 sec, followed by a 10-ml saline flush at a rate of 1 ml/sec. The delay time of the start of the angiography data acquisition was calculated (31) based on the transit time of the bolus in the perfusion imaging. For all the animals studied, an 8-sec delay between the start of injection and the start of data acquisition yielded a large enhancement of the pulmonary arteries.

For evaluating perfusion images semiquantitatively, parameter maps of lung perfusion were created, i.e., slope, maximum intensity, and time delay maps (defined below) (32). The images were first transferred to a remote SUN SPARC 20 workstation (Sun Microsystems, Mountain View, CA) and analyzed with a user-written program. An image mask was used to filter out background noise based on empirically defined threshold values. A perfusion curve for each pixel was then determined by the program. Four parameters from each curve were generated automatically: the maximum signal intensity SI_{max}, the time t_{max} of maximum signal, the signal intensity SI_{min} at the arrival of contrast agent (selected to be the intensity of the image when the next image intensity was 30% higher than the baseline image intensity SI_0), and the time t_{min} corresponding to SI_{min}. The baseline SI_0 was calculated by averaging the signal intensities on the first two images. Maps of the parameters were obtained by the formulae: slope = $(SI_{max} - SI_{min})/(t_{max}-t_{min})$, maximum signal = $SI_{max} - SI_0$, and time delay = $t_{max} - t_{min}$.

MR Helium Ventilation Imaging

Hyperpolarized ^{3}He gas is prepared by depopulation optical pumping of Rb and spin exchange between the Rb electrons and ^{3}He nuclei (33). A 40-W diode laser array was used to polarize the ^{3}He in valved Pyrex cells with equipment constructed by our research group. There are three dedicated polarizers; each generates 0.45L STP ^{3}He at approximately 45% polarization. The cells are then transported 4 km to the imager in a hand-carried, battery-powered holding field of 30 G; negligible losses occur during transport. However, care must be taken near the large field gradients close to the imager to avoid significant demagnetization of the gas (34).

The ventilation portion of imaging was performed on a 1.5 T Magnetom Vision whole-body scanner (Siemens Medical Systems) with a Helmholtz coil pair operating at 48.47 MHz and 63.63 MHz for ^{3}He and protons, respectively.

The Vision scanner was used for its multinuclear capability for ^{3}He imaging, although its lower performance gradient system is not suitable for the proton perfusion and angiography measurements. A complete set of coronal proton images is taken at full inspiration for comparison to the gas-space images and for anatomical reference. Just before ^{3}He imaging, the ^{3}He gas is mixed with 0.5 L N_2 in a polyethylene bag. The gas is delivered to the animal through a set of valves connected to the Harvard ventilator. When the imager has been switched to the ^{3}He frequency, 0.3 L of gas is first removed from the lungs at functional residual capacity by opening a valve to a partially evacuated plastic container. This removes some O_2, reducing the oxygen-induced relaxation rate of the ^{3}He (35). The 1-L ^{3}He-N_2 mixture is then delivered by opening a valve to the mixture and squeezing the polyethylene bag at a constant pressure of about 10 inches of water. At full inspiration all valves are closed to suspend breathing and imaging begins.

To image ^{3}He gas, a 2D gradient-echo sequence was used. Thirteen slices with a slice thickness of 8 mm were collected during a 13-sec breathhold. These slices were placed in similar locations as in the perfusion study. Other imaging parameters included: TR/TE = 11 ms/4.2 ms, flip angle = 15°, readout bandwidth = 130 Hz/pixel, FOV = 320 × 240 mm^2, data acquisition matrix = 128 × 96, resulting in a voxel size of 2.5 × 2.5 mm^2.

Imaging Protocol—All studies were first performed in the Sonata system for perfusion and angiographic imaging. Figure 1 shows the time diagram for the imaging procedure. After

acquiring baseline perfusion and angiography imaging data, the emboli or airway blockage was introduced and the same perfusion and angiography data acquisition procedures were repeated. The pig was then immediately transferred to the adjacent Vision system. ^{3}He gas imaging was performed there to visualize the lung ventilation distribution and detect any airway abnormalities.

RESULTS

Of 16 detected perfusion abnormalities in the five pigs, 11 defects were in the right lung and five in the left. However, postemboli MR angiograms were able to detect 20 emboli; the four emboli that were not distinguished in perfusion MR scans were obscured by other nearby emboli. It is noted that some angiographic images show accompanying parenchymal enhancements and abnormalities that were also demonstrated in the perfusion images. Nevertheless, the parenchymal signal enhancement in angiographic images is much less than in the perfusion images because the time delay between contrast injection and the start of angiographic imaging was selected to match the arterial phase of the contrast agent, not the parenchymal phase. The SNR of the parenchyma in the perfusion images is twice that of the angiographic images.

Figure 2 presents images from a pig pre- (top row) and postdelivery (bottom row) of blood clots to induce pulmonary embolism. The animal was injected with six emboli of lengths 2-6 cm. The postemboli perfusion image (Fig. 2c) reveals loss of signals in the right lateral lower lung and left middle to lower lung (compared to Fig. 2a). The postemboli angiographic image (Fig. 2d) clearly demonstrates the pulmonary arteries up to subsegmental branches. Cut-off vessels are shown in the distal portions of both right and left pulmonary arteries (compared to Fig. 2b). Additional small emboli in the left segmental and subsegmental branches are readily distinguished as cut-off defects. Despite the presence of such multiple emboli, the postemboli ^{3}He image shows perfectly normal ventilation throughout the lung. This observation of mismatched defects (perfusion/ventilation) is expected for pulmonary embolism.

Images from a pig pre- (top row) and postinflation (bottom row) of a balloon catheter to occlude an airway are displayed in Fig. 3. Preventilation-defect perfusion and angiographic imaging were performed and then the airway of the animal in the lower right lobe was obstructed by balloon angioplasty (Fig. 3d). Reduced perfusion is indicated (Fig. 3e) in the right lower lobe in the postventilation-defect image at the peak of arterial enhancement. The subsequent ^{3}He ventilation image (Fig. 3h) clearly shows a ventilation defect with similar shape and size of abnormality at the same location. Parametric images were also calculated from the perfusion datasets. Maximum intensity (Fig. 3b) and time delay (Fig. 3c) maps show the normal uniform signal patterns in the preventilation-defect case. The postventilation-defect maximum intensity map (Fig. 3f) continues to present a normal uniform distribution of signal. However, the postdefect time delay map (Fig. 3g) reveals delayed enhancement (hyperintensity) of the parenchyma distal to the balloon due to hypoxic vasoconstriction.

DISCUSSION AND CONCLUSIONS

With the help of the high-performance gradient system, our results demonstrate the feasibility of acquiring volumetric lung images within a reasonable breathhold time. First-pass volumetric perfusion imaging clearly delineated the blood perfusion of the pulmonary parenchyma, with lobar and segmental arterial and venous vessels demonstrated as well. Identification of these vessels is greatly assisted by viewing the images in 3D (slice thickness of 2.7 mm) with knowledge of the vascular structure of the pig lung. Therefore, this perfusion technique can provide low-spatial-resolution parenchymal perfusion maps and pulmonary angiography

simultaneously. However, high-spatial-resolution pulmonary angiography is still needed in some cases to allow accurate delineation of sources of pulmonary flow defects because our perfusion maps reveal "cut-off" signal voids only in large vessels. The exact location and extent of the emboli remain uncertain using only perfusion maps. With submillimeter resolution the angiography with a second contrast injection readily determines the locations and sizes of the small emboli, as shown in Fig. 2. Subsegmental branches are also well depicted (Fig. 2b,d).

It could be argued that high-spatial-resolution angiographic images may provide the same information as perfusion images. In our study, parenchymal perfusion was better delineated in the perfusion imaging, particularly in the nondefective regions. Angiographic images may present signal enhancement both in the vessels and parenchyma, but the SNR of the parenchyma is substantially lower than that in the perfusion images. Furthermore, variability of timing of the data acquisition window after contrast injection for the first-pass angiographic imaging will cause substantial variations in the parenchyma enhancement patterns, which may increase the possibility of false-positive diagnosis.

It is noted that related work was reported (27) in which lung ventilation was assessed indirectly with inhalation of 100% oxygen as a paramagnetic T_1 relaxation contrast agent. Ventilation/perfusion mismatch was observed using a pulmonary emboli animal model and proton MRI. This technique is less expensive and more readily available, as it can be performed on any proton MRI scanner and does not require ^{3}He polarized gas. However, only one slice was obtained with each oxygen inhalation and the SNR of the ventilation image is much lower. Other limitations include relatively long imaging time and the inability to perform dynamic ventilation imaging. In contrast, hyperpolarized ^{3}He MR lung imaging provides excellent SNR for visualizing the air space with multislice volume coverage within a single breathhold time and readily depicts the regional ventilation defects caused by stenosis of airways.

The corresponding perfusion defects matched the size and shape of the ventilation defects very well. Without involvement of ionizing radiation or iodinated contrast injection, the imaging approach presented here can be repeated and performed before and after an intervention. Although our current data acquisitions are performed in two scanners, the Sonata system will be upgraded with broadband capability in the near future, allowing all of the imaging (perfusion, angiography, and ^{3}He ventilation) to be performed in one setting. A single coronal slab could cover both right and left lungs without complex slice localization. This volumetric data acquisition strategy allows easy imaging set-up and also permits simple registration of perfusion, angiography, and ventilation images, even though the resolutions of the three image sets are different.

In conclusion, the described method of integration of MR angiography, perfusion, and ventilation imaging allows delineation of lung anatomy and function in the blood and air space in one setting. This approach appears sensitive to pulmonary vascular and bronchial stenosis. Non- or less-perfused and nonventilated lung regions can be readily detected and characterized with the volumetric datasets. However, the accuracy, sensitivity, and specificity of the integration of the three imaging methods needs further evaluation in a larger number of subjects. The clinical utility must also be evaluated.

Acknowledgements

Grant sponsor: Radiological Society of North America.

REFERENCES

1. Hatabu, H.; Alsop, D.; Bonnet, M.; Listerud, J.; Pietra, G.; Gefter, W. Approaches to MR imaging of lung parenchyma utilizing ultrashort TE gradient echo and fast SE sequences; Proc 2nd Annual Meeting SMR; San Francisco. 1994; p. 1474
2. Alsop DC, Hatabu H, Bonnet M, Listerud J, Gefter W. Multi-slice, breathhold imaging of the lung with submillisecond echo times. Magn Reson Med 1995;33:678–682. [PubMed: 7596272]
3. Hatabu H, Gaa J, Kim D, Li W, Prasad PV, Edelman RR. Pulmonary perfusion: qualitative assessment with dynamic contrast-enhanced MRI using ultra-short TE and inversion recovery turbo FLASH. Magn Reson Med 1996;36:503–508. [PubMed: 8892200]
4. Berthezene Y, Croisille P, Wiart M, Howarth N, Houzard C, Faure O, Douek P, Amiel M, Revel D. Prospective comparison of MR lung perfusion and lung scintigraphy. J Magn Reson Imag 1999;9:61–68.
5. Schoenberg SO, Bock M, Floemer F, Grau A, Williams DM, Laub G, Knopp MV. High-resolution pulmonary arterio- and venography using multiple-bolus multiphase 3D-Gd-mRA. J Magn Reson Imag 1999;10:339–346.
6. Hatabu H, Tadamura E, Levin DL, Chen Q, Li W, Kim D, Prasad PV, Edelman RR. Quantitative assessment of pulmonary perfusion with dynamic contrast-enhanced MRI. Magn Reson Med 1999;42:1033–1038. [PubMed: 10571924]
7. Carr, J.; Laub, G.; Saker, M.; Zheng, J.; Pereles, S.; Tatieni, S.; Finn, JP. Time-resolved pulmonary MR angiography and perfusion imaging with ultrashort TR; Proc 8th Annual Meeting ISMRM; Denver. 2000; p. 72
8. Viallon, M.; Schreiber, W.; Heussel, CP.; Mohrs, O.; Schmitt, M.; Gast, KK.; Eberle, B.; Thelen, M.; Kauczor, HU. Absolute quantification of pulmonary perfusion using dynamic T1 contrast enhanced MRI: estimation of regional pulmonary blood flow (rPBF) and blood volume (rPBV); Proc 9th Annual Meeting ISMRM; Glasgow, Scotland. 2001; p. 186
9. Kveder M, Zupancic I, Lahajnar G, Blinc R, Suput D, Ailion DC, Ganesan K, Goodrich C. Water proton NMR relaxation mechanisms in lung tissue. Magn Reson Med 1988;7:432–441. [PubMed: 3173058]
10. Hatabu H, Gaa J, Kim D, Li W, Prasad PV, Edelman RR. Pulmonary perfusion and angiography: evaluation with breath-hold enhanced three-dimensional fast imaging steady-state precession MR imaging with short TR and TE. Am J Roentgenol 1996;167:653–655. [PubMed: 8751673]
11. Hatabu H, Alsop DC, Listerud J, Bonnet M, Gefter WB. T2* and proton density measurement of normal human lung parenchyma using submillisecond echo time gradient echo magnetic resonance imaging. Eur J Radiol 1999;29:245–252. [PubMed: 10399610]
12. Stock KW, Chen Q, Hatabu H, Edelman RR. Magnetic resonance T2* measurements of the normal human lung in vivo with ultra-short echo times. Magn Reson Imag 1999;17:997–1000.
13. Steiner P, McKinnon GC, Romanowski B, Goehde SC, Hany T, Debatin JF. Contrast-enhanced, ultrafast 3D pulmonary MR angiography in a single breath-hold: initial assessment of imaging performance. J Magn Reson Imag 1997;7:177–182.
14. Meaney JF, Weg JG, Chenevert TL, Stafford-Johnson D, Hamilton BH, Prince MR. Diagnosis of pulmonary embolism with magnetic resonance angiography. N Engl J Med 1997;336:1422–1427. [PubMed: 9145679]
15. Gupta A, Frazer CK, Ferguson JM, Kumar AB, Davis SJ, Fallon MJ, Morris IT, Drury PJ, Cala LA. Acute pulmonary embolism: diagnosis with MR angiography. Radiology 1999;210:353–359. [PubMed: 10207414]
16. Amundsen T, Kvaerness J, Aadahl P, Waage A, Bjermer L, Odegard A, Haraldseth O. A closed-chest pulmonary artery occlusion/reperfusion model in the pig: detection of experimental pulmonary embolism with MR angiography and perfusion MR imaging. Invest Radiol 2000;35:295–303. [PubMed: 10803670]
17. Middleton H, Black RD, Saam B, Cates GD, Cofer GP, Guenther R, Happer W, Hedlund LW, Johnson GA, Juvan K, Swartz J. MR imaging with hyperpolarized ^{3}He gas. Magn Reson Med 1995;33:271–275. [PubMed: 7707920]

18. MacFall JR, Charles HC, Black RD, Middleton H, Swartz JC, Saam B, Driehuys B, Erickson C, Happer W, Cates GD, Johnson GA, Ravin CE. Human lung air spaces: potential for MR imaging with hyperpolarized He-3. Radiology 1996;200:553–558. [PubMed: 8685356]
19. Kauczor HU, Hofmann D, Kreitner KF, Nilgens H, Surkau R, Heil W, Potthast A, Knopp MV, Otten EW, Thelen M. Normal and abnormal pulmonary ventilation: visualization at hyperpolarized He-3 MR imaging. Radiology 1996;201:564–567. [PubMed: 8888259]
20. Chen XJ, Chawla MS, Hedlund LW, Moller HE, MacFall JR, Johnson GA. MR microscopy of lung airways with hyperpolarized ^{3}He. Magn Reson Med 1998;39:79–84. [PubMed: 9438440]
21. Saam BT, Yablonskiy DA, Gierada DS, Conradi MS. Rapid imaging of hyperpolarized gas using EPI. Magn Reson Med 1999;42:507–514. [PubMed: 10467295]
22. de Lange EE, Mugler JP 3rd, Brookeman JR, Knight-Scott J, Truwit JD, Teates CD, Daniel TM, Bogorad PL, Cates GD. Lung air spaces: MR imaging evaluation with hyperpolarized ^{3}He gas. Radiology 1999;210:851–857. [PubMed: 10207491]
23. Saam BT, Yablonskiy DA, Kodibagkar VD, Leawoods JC, Gierada DS, Cooper JD, Lefrak SS, Conradi MS. MR imaging of diffusion of ^{3}He gas in healthy and diseased lungs. Magn Reson Med 2000;44:174–179. [PubMed: 10918314]
24. Altes TA, Powers PL, Knight-Scott J, Rakes G, Platts-Mills TA, de Lange EE, Alford BA, Mugler JP 3rd, Brookeman JR. Hyperpolarized ^{3}He MR lung ventilation imaging in asthmatics: preliminary findings. J Magn Reson Imag 2001;13:378–384.
25. Edelman R, Hatabu H, Tadamura E, Li W, Prasad P. Noninvasive assessment of regional ventilation in the human lung using oxygen-enhanced magnetic resonance imaging. Nat Med 1996;2:1236–1239. [PubMed: 8898751]
26. Chen Q, Jakob P, Griswold M, Levin D, Hatabu H, Edelman R. Oxygen enhanced MR ventilation imaging of the lung. MAGMA 1998;7:153–161. [PubMed: 10050941]
27. Chen Q, Levin DL, Kim D, David V, McNicholas M, Chen V, Jakob PM, Griswold MA, Goldfarb JW, Hatabu H, Edelman RR. Pulmonary disorders: ventilation-perfusion MR imaging with animal models. Radiology 1999;213:871–879. [PubMed: 10580969]
28. Viallon M, Berthezene Y, Decorps M, Wiart M, Callot V, Bourgeois M, Humblot H, Briguet A, Cremillieux Y. Laser-polarized ^{3}He as a probe for dynamic regional measurements of lung perfusion and ventilation using magnetic resonance imaging. Magn Reson Med 2000;44:1–4. [PubMed: 10893513]
29. Cremillieux Y, Berthezene Y, Humblot H, Viallon M, Canet E, Bourgeois M, Albert T, Heil W, Briguet A. A combined ^{1}H perfusion / ^{3}He ventilation NMR study in rat lungs. Magn Reson Med 1999;41:645–648. [PubMed: 10332838]
30. Brink JA, Woodard PK, Horesh L, Heiken JP, Glazer HS, Anderson DC, Wang G, Schwartz DM. Depiction of pulmonary emboli with spiral CT: optimization of display window settings in a porcine model. Radiology 1997;204:703–708. [PubMed: 9280246]
31. Earls JP, Rofsky NM, DeCorato DR, Krinsky GA, Weinreb JC. Breathhold single-dose gadolinium-enhanced three-dimensional MR aortography: usefulness of a timing examination and MR power injector. Radiology 1996;201:705–710. [PubMed: 8939219]
32. Penzkofer H, Wintersperger BJ, Knez A, Weber J, Reiser M. Assessment of myocardial perfusion using multisection first-pass MRI and color-coded parameter maps: a comparison to 99mTc Sesta MIBI SPECT and systolic myocardial wall thickening analysis. Magn Reson Imag 1999;17:161–170.
33. Walker TG, Happer W. Spin-exchange optical pumping of noble-gas nuclei. Rev Mod Phys 1997;69:629–642.
34. Cates GD, Schaefer SR, Happer W. Relaxation of spins due to field inhomogeneities in gaseous samples at low magnetic fields and at low pressures. Phys Rev A 1988;37:2877–3885. [PubMed: 9900016]
35. Moeller HE, Hedlund LW, Chen XJ, Carey MR, Chawla MS, Wheller CT, Johnson GA. Measurements of hyperpolarized gas properties in the lung. III. ^{3}He T_1. Magn Reson Med 2001;45:421–430. [PubMed: 11241699]

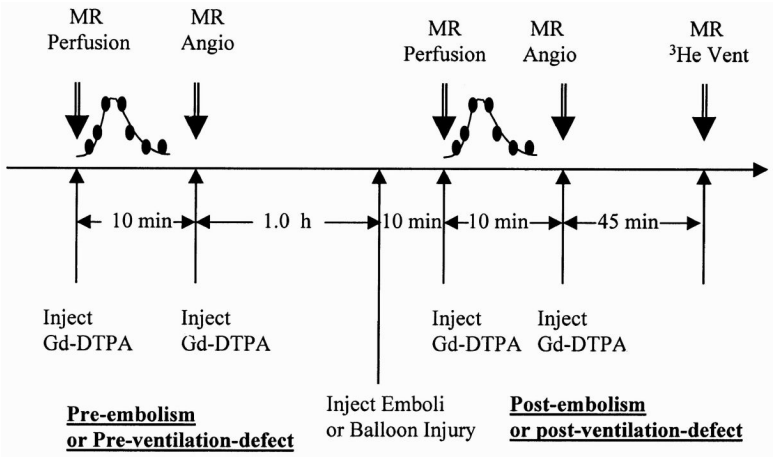

FIG. 1.

Schematic diagram of time-line of imaging procedures for the integration of MR scans. There was a 1-hr delay between the preemboli and postemboli studies to ensure residual contrast agent would not significantly interfere with the postemboli imaging.

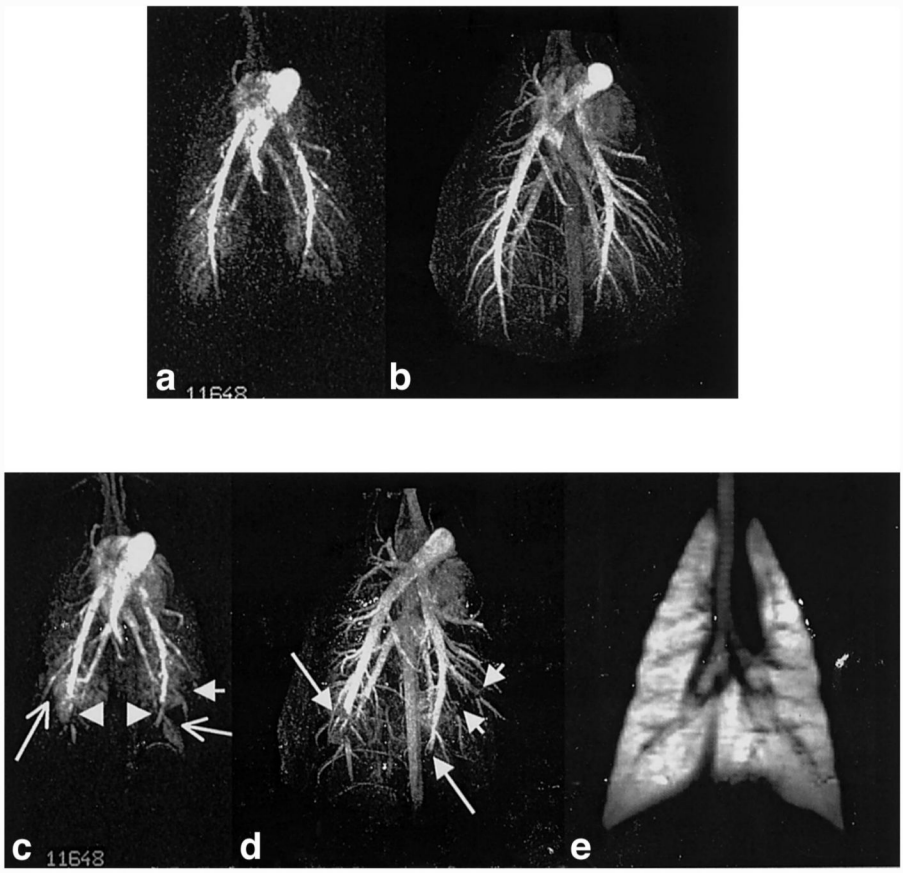

FIG. 2.

Images from lungs of a pig pre-injection (top row) and postinjection (bottom row) of pulmonary emboli in the form of blood clots. Perfusion images **a** and **c** are reconstructed from a 3D dataset using MIP. The two long arrows in image **c** indicate multiple parenchymal perfusion abnormalities induced by the two emboli, as indicated by arrowheads. Main and both right and left lobar pulmonary arteries are also visualized. Images **b** and **d** are high-resolution MR angiography (MIP), clearly showing the smaller subsegmental and even subsubsegmental vessels. In **d**, emboli are marked by arrows. Note two short arrows in **d** point to two subsegmental emboli which are not seen in perfusion image **c** (short arrow). Image **e** is a single slice from ^{3}He and shows normal ventilation distribution of the lung postemboli with high SNR.

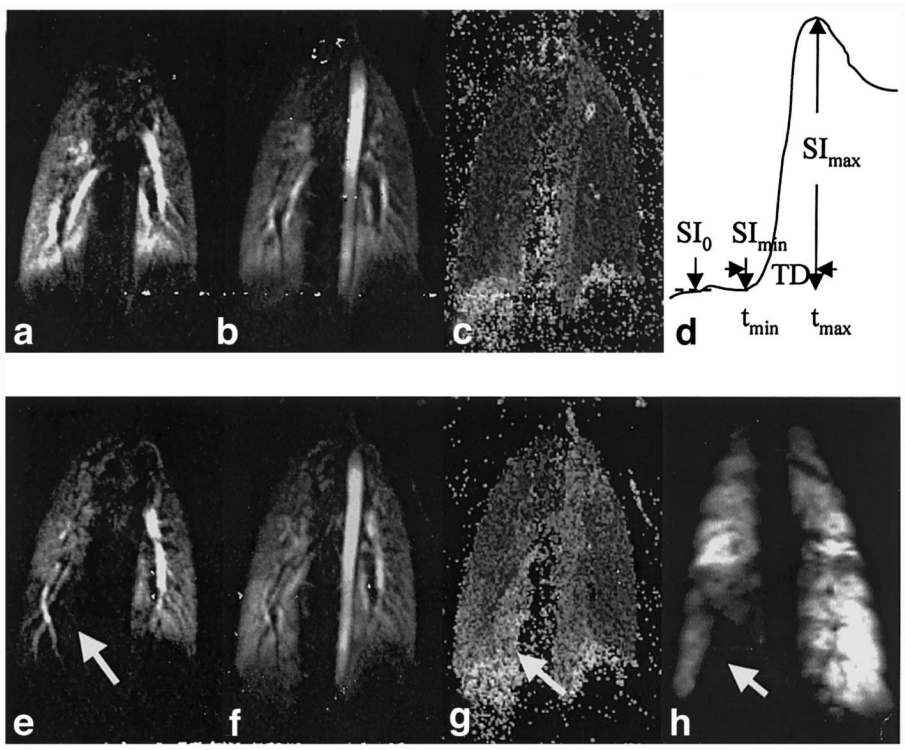

FIG. 3.

Images from lungs of a pig before (top row) and after (bottom row) creation of a ventilation defect. Images **a** and **e** are one slice from a 3D perfusion dataset. Images **b** and **f** are maximum intensity images (SI_{max}) calculated from the dynamic perfusion datasets. Images **c** and **g** are time delay maps, as defined in the text, with hyperintensity representing longer delays. Image **d** schematically illustrates the definitions of the parameters in the calculated parametric maps. Image **h** was acquired postventilation-defect using ^{3}He. The arrow in **e**, **g**, and **h** points to the region of defective ventilation.